








## Detection of current-sheet and bipolar ion flows in a self-generated antiparallel magnetic field of laser-produced plasmas for magnetic reconnection research

T. Morita <sup>1,\*</sup>, T. Kojima,<sup>2</sup> S. Matsuo,<sup>2</sup> S. Matsukiyo <sup>1,3</sup>, S. Isayama <sup>1</sup>, R. Yamazaki <sup>4,5</sup>, S. J. Tanaka <sup>4</sup>, K. Aihara,<sup>4</sup> Y. Sato,<sup>4</sup> J. Shiota,<sup>4</sup> Y. Pan,<sup>2</sup> K. Tomita,<sup>6</sup> T. Takezaki,<sup>7</sup> Y. Kuramitsu,<sup>8</sup> K. Sakai <sup>8</sup>, S. Egashira,<sup>9</sup> H. Ishihara,<sup>9</sup> O. Kuramoto,<sup>9</sup> Y. Matsumoto,<sup>9</sup> K. Maeda,<sup>9</sup> and Y. Sakawa <sup>5</sup>

<sup>1</sup>*Faculty of Engineering Sciences, Kyushu University, 6-1 Kasuga-Koen, Kasuga, Fukuoka 816-8580, Japan*

<sup>2</sup>*Interdisciplinary Graduate School of Engineering Sciences, Kyushu University, 6-1, Kasuga-Koen, Kasuga, Fukuoka 816-8580, Japan*

<sup>3</sup>*International Research Center for Space and Planetary Environmental Science, Kyushu University, Motooka, Nishi-Ku, Fukuoka 819-0395, Japan*

<sup>4</sup>*Department of Physical Sciences, Aoyama Gakuin University, 5-10-1 Fuchinobe, Sagami-hara, Kanagawa 252-5258, Japan*

<sup>5</sup>*Institute of Laser Engineering, Osaka University, 2-6 Yamadaoka, Suita, Osaka 565-0871, Japan*

<sup>6</sup>*Faculty of Engineering, Hokkaido University, Kita 13 Nishi 8, Kita-ku, Sapporo 060-8628, Japan*

<sup>7</sup>*Faculty of Engineering, University of Toyama, Gofuku 3190, Toyama-shi, Toyama 930-8555, Japan*

<sup>8</sup>*Graduate School of Engineering, Osaka University, 2-1 Yamadaoka, Suita, Osaka 565-0871, Japan*

<sup>9</sup>*Graduate School of Science, Osaka University, 1-1 Machikane-yama, Toyonaka, Osaka 560-0043, Japan*



(Received 31 May 2022; accepted 23 September 2022; published 10 November 2022)

Magnetic reconnection in laser-produced magnetized plasma is investigated by using optical diagnostics. The magnetic field is generated via the Biermann battery effect, and the inversely directed magnetic field lines interact with each other. It is shown by self-emission measurement that two colliding plasmas stagnate on a midplane, forming two planar dense regions, and that they interact later in time. Laser Thomson scattering spectra are distorted in the direction of the self-generated magnetic field, indicating asymmetric ion velocity distribution and plasma acceleration. In addition, the spectra perpendicular to the magnetic field show different peak intensity, suggesting an electron current formation. These results are interpreted as magnetic field dissipation, reconnection, and outflow acceleration. Two-directional laser Thomson scattering is, as discussed here, a powerful tool for the investigation of microphysics in the reconnection region.

DOI: [10.1103/PhysRevE.106.055207](https://doi.org/10.1103/PhysRevE.106.055207)

### I. INTRODUCTION

Magnetic reconnection in collisionless plasma plays a key role in global change of magnetic field topology and rapid energy conversion from magnetic field to plasma thermal and kinetic energies [1,2]. The reconnection physics includes both microscopic magnetic-field dissipation in an electron scale, and macroscopic field advection in surrounding plasmas. This large-scale difference makes it difficult to understand the whole story of magnetic reconnection. Laser-plasma experiments can be a useful tool for investigating magnetic reconnection, especially in high- $\beta$  condition. Strong magnetic field is, spontaneously, generated in a high-temperature and high-speed expanding plasma via laser-solid interaction, and an antiparallel field structure is easily formed by the laser irradiation of two different spots [3–6]. However, local measurements of plasma parameters and magnetic field are difficult in such small-scale and fast-expanding plasmas and, so far, there have been few discussions on current-sheet formation, inflow and outflow parameters, plasma energization, and reconnection rate.

Recently, laser-produced plasmas have been precisely measured with laser Thomson scattering (LTS) [5,7–9]. The spectral shape of the ion feature is explained as a result of ion acoustic resonance and Landau damping on an ion acoustic wave depending on ion and electron velocity distributions. Typical plasma parameters such as temperature, density, average charge state, and flow velocity can be obtained in the case of Maxwellian velocity distribution. However, the velocity distributions can be asymmetric in nonequilibrium plasma, such as in a shock transition region, current sheet, and magnetic reconnection region. Even when ions are in non-Maxwellian distribution, the ion distribution function is inferred considering the different damping effects on positive and negative phase velocities, or blue- and redshifted resonance peaks of the scattered spectrum.

In this paper, we report the measurement of appearance and disappearance of an electron current sheet accompanied by bidirectional ion outflows in the time evolution of magnetic reconnection occurring between laser-produced magnetized plasmas. The self-emission (SE) imaging shows the interaction of two laser-produced plasmas. Two plasmas stagnate in an antiparallel self-generated magnetic field and they connect with each other later in time, suggesting a sudden decrease in the magnetic pressure. The resonant peaks of the ion feature, almost perpendicular to the self-generated magnetic field,  $\mathbf{B}$ ,

\*morita@aes.kyushu-u.ac.jp

show asymmetry in height, suggesting electron drift relative to ions or asymmetric electron velocity distribution—in other words, an electron current formation. The asymmetry in the spectrum decreases later in time, which means symmetric velocity distribution on both electrons and ions. This fact indicates the disappearance of the electron current. The ion feature parallel to  $\mathbf{B}$  shows different widths on blue- and redshifted peaks, indicating asymmetric ion velocity distribution or bidirectional ion flows depending on the position. The appearance and disappearance of the electron current and bipolar ion flows are interpreted as the magnetic-field dissipation in the current sheet, magnetic reconnection, and resultant outflow jets.

In Sec. II, we briefly review the theory of LTS with Maxwellian and non-Maxwellian electron and ion velocity distributions. The experimental observation of asymmetric ion features and the interpretations of these spectra with non-Maxwellian velocity distributions are shown in Sec. III. In addition, we discuss the existence of bipolar ion flows and electron current in the antiparallel magnetic field in Sec. IV, and we summarize the analysis and discussion in Sec. V.

## II. LASER THOMSON SCATTERING IN THE CASE OF NON-MAXWELLIAN ELECTRON AND ION DISTRIBUTIONS

### A. LTS spectrum for Maxwellian velocity distribution

The LTS spectrum is expressed with the spectral density function [10],

$$S(k, \omega) = \frac{2\pi}{k} \left[ \left| 1 - \frac{\chi_e}{\epsilon} \right|^2 f_e \left( \frac{\omega}{k} \right) + \sum_j \frac{Z_j^2 n_j}{n_e} \left| \frac{\chi_e}{\epsilon} \right|^2 f_j \left( \frac{\omega}{k} \right) \right], \quad (1)$$

where  $j$  is the ion species,  $\mathbf{k} = \mathbf{k}_s - \mathbf{k}_i$  and  $\omega = \omega_s - \omega_i$  are the wave number and frequency of the plasma wave, respectively,  $\mathbf{k}_i$  and  $\mathbf{k}_s$  are the wave numbers of incident and scattered light, respectively,  $\omega_i$  and  $\omega_s$  are the frequencies of incident and scattered light, respectively, and  $\epsilon$  and  $\chi_e$  are longitudinal dielectric function and electron susceptibility, respectively, shown below:

$$\epsilon = 1 + \chi_e + \sum_j \chi_j, \quad (2)$$

$$\chi_e = \frac{e^2 n_e}{m_e \epsilon_0 k} \int \frac{\partial f_e / \partial v}{\omega - kv} dv, \quad (3)$$

$$\chi_j = \frac{Z_j^2 e^2 n_j}{m_j \epsilon_0 k} \int \frac{\partial f_j / \partial v}{\omega - kv} dv. \quad (4)$$

$Z_j$  is the average charge state of ions, and  $f_e$  and  $f_j$  are the electron and ion velocity distributions, respectively. In the case of Maxwellian distribution,  $f$  is expressed below:

$$f(v) = \frac{1}{\sqrt{\pi} v_{\text{th}}} \exp \left( -\frac{(v - v_f)^2}{v_{\text{th}}^2} \right). \quad (5)$$

Here,  $v_f$  is the flow velocity in the  $\mathbf{k}$  direction, and  $v_{\text{th}}$  is the thermal velocity of species:

$$v_{\text{th},e} = \sqrt{\frac{2T_e}{m_e}} \quad \text{and} \quad v_{\text{th},j} = \sqrt{\frac{2T_j}{m_j}}. \quad (6)$$

When both the ions and electrons are in a Maxwellian distribution,  $S(k, \omega)$  becomes

$$S(k, \omega) = \frac{2\sqrt{\pi}}{k} \left[ \frac{1}{v_{\text{th},e}} \left| 1 - \frac{\chi_e}{\epsilon} \right|^2 e^{-\xi_e^2} + \sum_j \frac{1}{v_{\text{th},j}} \frac{Z_j^2 n_j}{n_e} \left| \frac{\chi_e}{\epsilon} \right|^2 e^{-\xi_j^2} \right], \quad (7)$$

where  $\xi_e$  and  $\xi_j$  are phase velocities normalized by the thermal velocities shown below:

$$\xi_e = (\omega/k - v_{fe})/v_{\text{th},e} \quad \text{and} \quad \xi_j = (\omega/k - v_{fj})/v_{\text{th},j}. \quad (8)$$

$\chi_e$  and  $\chi_j$  become

$$\chi_e = \frac{1}{k^2 \lambda_e^2} w(\xi_j) \quad \text{and} \quad \chi_j = \frac{1}{k^2 \lambda_j^2} w(\xi_j), \quad (9)$$

where

$$\lambda_e^2 = v_{\text{th},e}^2 / \omega_{pe}^2 = 2\epsilon_0 T_e / n_e e^2, \quad (10)$$

$$\lambda_j^2 = v_{\text{th},j}^2 / \omega_{pj}^2 = 2\epsilon_0 T_j / n_j Z_j^2 e^2, \quad (11)$$

and  $w$  is the derivative of the plasma dispersion function. In the case of single ion species, we have

$$S(k, \omega) = \frac{2\pi}{k} \left[ \left| 1 - \frac{\chi_e}{\epsilon} \right|^2 f_e \left( \frac{\omega}{k} \right) + Z_i \left| \frac{\chi_e}{\epsilon} \right|^2 f_i \left( \frac{\omega}{k} \right) \right], \quad (12)$$

or in Maxwellian distribution,

$$S(k, \omega) = \frac{2\sqrt{\pi}}{k} \left[ \frac{1}{v_{\text{th},e}} \left| 1 - \frac{\chi_e}{\epsilon} \right|^2 e^{-\xi_e^2} + \frac{Z_i}{v_{\text{th},i}} \left| \frac{\chi_e}{\epsilon} \right|^2 e^{-\xi_i^2} \right]. \quad (13)$$

### B. Maxwellian and non-Maxwellian electron velocity distributions

When the electron flow drifts from ion flow keeping their distributions Maxwellian, the LTS spectrum becomes asymmetric due to different rates of electron and ion Landau damping on the ion acoustic waves propagating in positive and negative  $\mathbf{k}$  directions (the left and right sides of the ion feature). Figure 1(a) shows the ion features of LTS with different electron drift  $v_{fe} = 0$  (solid line) and  $-0.02v_{\text{th},e}$  (dashed line). The corresponding velocity distributions are shown in Fig. 1(b) with solid and dashed lines, respectively. This asymmetric LTS spectrum can also be obtained when the electron velocity distribution is distorted and is no longer Maxwellian as shown with the dot-dashed line in Fig. 1(b). Here, the non-Maxwellian distribution is expressed with the summation of two different Maxwellian distributions:  $f = 0.5(f_1 + f_2)$  with different temperatures and drift velocities, and the same electron damping effects on the ion acoustic wave, indicating the same derivative of the distribution function  $\partial f / \partial v$  near the phase velocity of the ion acoustic wave.

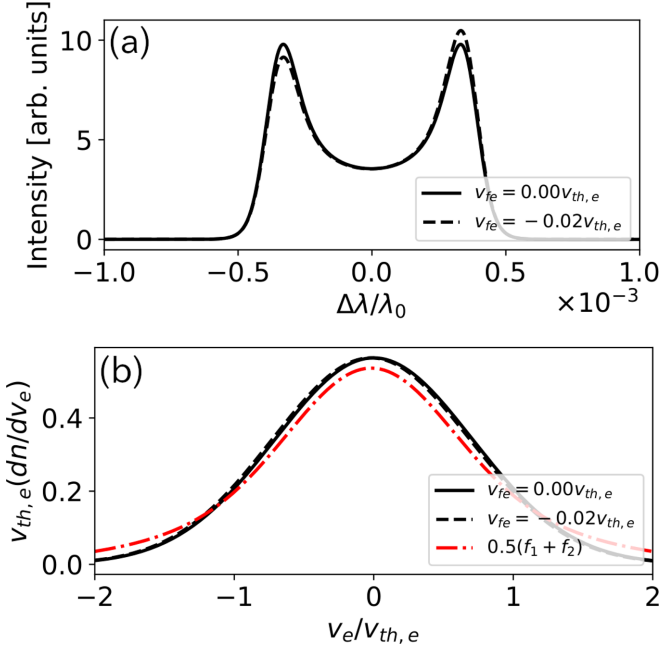


FIG. 1. (a) LTS spectra with two different electron drifts relative to ions:  $v_{fi} = 0$ ,  $v_{fe} = 0$  (solid line) and  $-0.02v_{th,e}$  (dashed line). (b) The electron velocity distributions with the flow velocities  $v_{fe} = 0$  (solid line) and  $v_{fe} = -0.02v_{th,e}$  (dashed line). A non-Maxwellian electron velocity distribution (dot-dashed line) reproduces the same spectrum of  $v_{fe} = -0.02v_{th,e}$  shown with dashed line in (a).

### C. Non-Maxwellian ion velocity distribution

When the ion velocity distribution is not expressed as Maxwellian, the ion susceptibility is not so simple, and an ion feature is affected by different Landau damping on left and right peaks depending on ion and electron velocity distributions, which has been experimentally observed [11,12] and numerically calculated [13] for two streaming plasmas. We assume that the non-Maxwellian ion distribution  $f_i$  is the sum of two different Maxwellian distributions with different temperatures as follows:

$$f_i = \alpha f_{i1} + (1 - \alpha) f_{i2}, \quad (14)$$

where  $\alpha$  is the abundance ratio. The ion susceptibility  $\chi_i$  becomes

$$\chi_i = \alpha \chi_{i1} + (1 - \alpha) \chi_{i2}, \quad (15)$$

and the LTS spectrum  $S(k, \omega)$  is given by

$$S(k, \omega) = \frac{2\sqrt{\pi}}{k} \left[ \frac{1}{v_{th,e}} \left| 1 - \frac{\chi_e}{\epsilon} \right|^2 e^{-\xi_e^2} + \frac{\alpha Z_1}{v_{th,1}} \left| \frac{\chi_e}{\epsilon} \right|^2 e^{-\xi_1^2} + \frac{(1 - \alpha) Z_2}{v_{th,2}} \left| \frac{\chi_e}{\epsilon} \right|^2 e^{-\xi_2^2} \right], \quad (16)$$

as shown in Fig. 2(a). We assume that electrons are in a Maxwellian distribution, and that there is no effective current:  $v_{fe} n_e = \alpha Z_1 n_{i1} v_{f1} + (1 - \alpha) Z_2 n_{i2} v_{f2}$ . Note that the ion feature shown in Fig. 2(a) does not strongly depend on the electron flow velocity in  $0 < |v_{fe}| \lesssim |v_{f2}|$ . Figure 2(b) shows

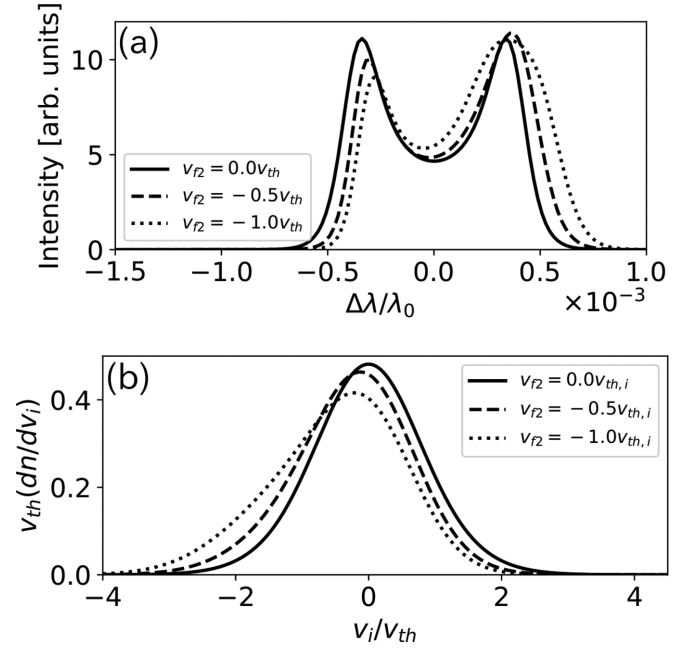


FIG. 2. (a) LTS spectra for non-Maxwellian ion velocity distributions of  $f = f_1 + f_2$ , where  $f_1$  and  $f_2$  are Maxwellian distributions with different temperatures and drift velocities  $v_{f2} = 0$ ,  $-0.5v_{th,i}$ , and  $-v_{th,i}$  (shown with solid, dashed, and dotted lines, respectively). The corresponding velocity distributions are shown in (b).

the ion velocity distributions with  $\alpha = 0.5$ ,  $T_{i1} = 100$  eV, and  $T_{i2} = 300$  eV,

$$f_{i1}(v) = \frac{1}{\sqrt{\pi} v_{th,1}} \exp\left(-\frac{(v - v_{f1})^2}{v_{th,1}^2}\right), \quad (17)$$

$$f_{i2}(v) = \frac{1}{\sqrt{\pi} v_{th,2}} \exp\left(-\frac{(v - v_{f2})^2}{v_{th,2}^2}\right), \quad (18)$$

and the flow velocities of first and second flows:  $v_{f1} = 0$  and  $v_{f2} \neq 0$ . Here, three velocity distributions with different  $v_{f2}$  of 0,  $-0.5v_{th,i}$ , and  $-v_{th,i}$  are shown.

Unlike in the case of electron drift shown in Fig. 1, both the intensity and the width of the two resonant peaks change depending on  $T_{i1}$ ,  $T_{i2}$ ,  $v_f$ , and  $\alpha$ , and this asymmetric effect on each resonant peak allows us to infer rapid thermalization and acceleration such as the interaction of counterstreaming plasmas [11,14–17], shockwave generation [18–21], and magnetic reconnection [22–24].

### D. Modified spectrum measured with gated detector

In the case of experimental measurement, the spectrum is modified when the velocity changes in an exposure time of a detector. This effect is sometimes important for pulsed plasmas, for example, laser-produced plasmas, measured with a gated detector such as an intensified charge coupled device (ICCD) camera. The spectrum is modified by taking the average in  $v_f \pm \Delta v/2$  as

$$S_{\Delta v_f}(k, \omega) = \frac{1}{\Delta v_f} \int_{v_f - \Delta v/2}^{v_f + \Delta v/2} S(k, \omega) dv_f. \quad (19)$$

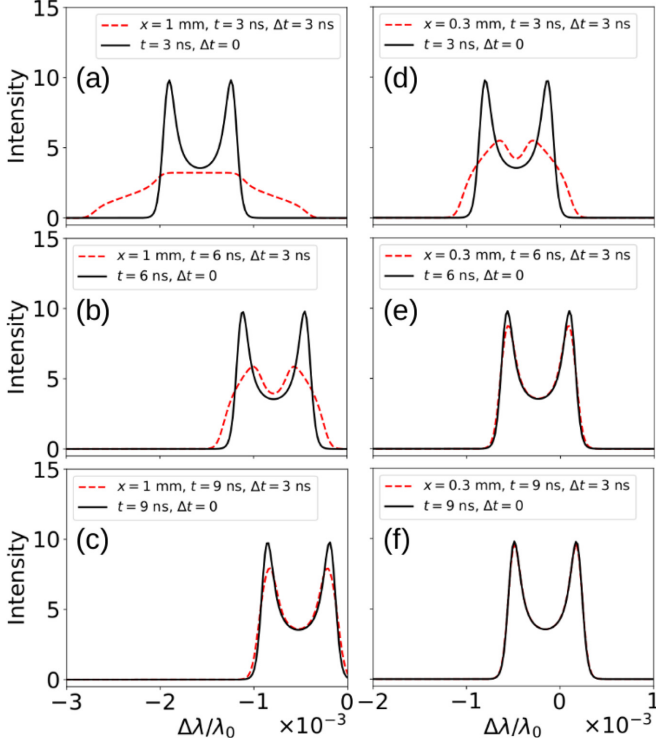


FIG. 3. The ion features of the LTS spectra calculated with Eq. (13) (solid line) and Eq. (19) (dashed line), with the measurement times [(a) and (d)]  $t = 3$  ns, [(b) and (e)]  $t = 6$  ns, and [(c) and (f)]  $t = 9$  ns, the exposure time  $\Delta t = 3$  ns, and measurement position of [(a)–(c)]  $x = 1$  mm and [(d)–(f)]  $x = 0.3$  mm. The carbon plasma is assumed with  $T_e = T_i = 100$  eV,  $n_e = 2 \times 10^{18}$  cm $^{-3}$ ,  $Z = 6$ , and  $v_f = x/t$ .

The flow velocity is typically expressed as  $v_f = x/t$ , where  $x$  is the distance and  $t$  is the time after the laser irradiation, and the flow velocity change in a gate width of  $\Delta t$  becomes  $\Delta v_f \sim v_f \Delta t/t$ . This modification can be ignored with small  $v_f$  and/or  $\Delta t/t \ll 1$ , but should be taken into account for fitting the measured spectrum with large  $v_f$  and  $\Delta t/t \gtrsim 1$ . Figures 3(a)–3(c) show the spectra of the ion features for carbon plasma with  $T_e = T_i = 100$  eV,  $n_e = 2 \times 10^{18}$  cm $^{-3}$ , and  $Z = 6$  at  $x = 1$  mm and at  $t = 3, 6,$  and  $9$  ns, respectively. Figures 3(d)–3(f) show the spectra calculated in the same way with the distance  $x = 0.3$  mm. The dashed lines show the velocity-averaged spectra calculated with Eq. (19) with the gate width  $\Delta t = 3$  ns which is comparable to the present experiment shown later. The velocity-averaged spectra (dashed lines) become close to the theoretical spectra ( $\Delta t = 0$ , solid lines) later in time in both cases of the distance  $x = 1$  and  $0.3$  mm. Even in the case of small  $\Delta t/t$  with  $x = 1$  mm, for example,  $\Delta t/t = 1/2$  [Fig. 3(b)] and  $1/3$  [Fig. 3(c)], the spectra are modified. On the other hand, with  $x = 0.3$  mm, the modification is small as shown in Figs. 3(e) and 3(f). Our spectral analyses in the following sections are done in the time range  $t = 5$ – $9$  ns and in the distance  $-0.3 < x < 3$  mm, and this velocity-averaged effect in a limited gate width is ignorable. Therefore, LTS spectra are fitted with the theoretical function without taking the average in velocity in the following sections.

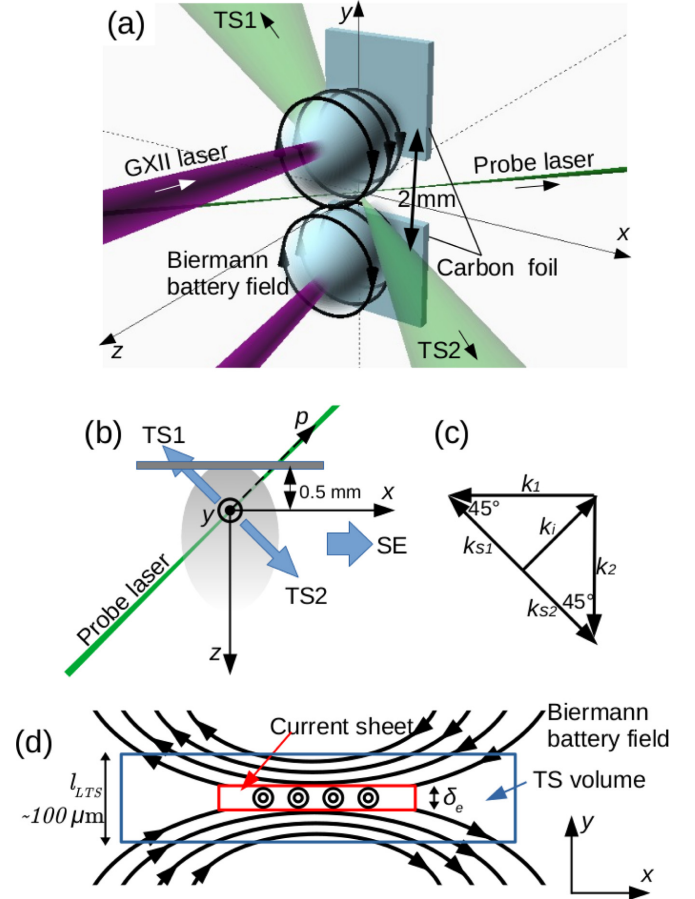


FIG. 4. (a) Schematic view of laser ablation, self-generated (Biermann battery) magnetic field, and LTS measurement. (b) The top view of the target showing the laser-produced plasma, probe laser, and Thomson scattering (TS) and SE measurements. (c) Two different TS measurement directions ( $k_1$  and  $k_2$ ). (d) The magnetic field structure on the  $xy$ -plane.

### III. EXPERIMENT

The experiment was performed with the Gekko-XII laser system at the Institute of Laser Engineering, Osaka University. Two laser beams with average energy of 700 J in 1.3 ns at a wavelength of 1053 nm were focused in a diameter of  $\sim 100$   $\mu$ m and irradiated two individual carbon planar foils with a thickness of 0.1 mm. Two foils were located at  $z = -0.5$  mm on the  $x$ - $y$  plane, and two spots were separated by 2 mm along the  $y$  axis as shown in Fig. 4(a). The strong magnetic field of  $B \sim 100$  T is self-generated due to the anisotropy of density and temperature gradients formed around the laser spots (Biermann battery effect [25],  $\partial \mathbf{B}/\partial t \propto \nabla T_e \times \nabla n_e$ ). As discussed later, laser-produced plasma has large plasma  $\beta$  ( $\beta_e = 2\mu_0 n_e T_e / B^2 \gg 1$ ), indicating that the magnetic field is advected along with freely expanding electron flux.  $\beta_e$  becomes small later in time, and  $\beta_e \lesssim 1$  when two plasmas interact at  $t \sim 5$ – $7$  ns. Two antiparallel magnetic-field lines interact at  $x \sim 0$  on the midplane,  $y = 0$ , as the plasma plumes expand. A similar experimental setup has recently been used for magnetic reconnection research with a high-power laser [3–6, 26–28], and the

current-sheet formation and magnetic reconnection have been investigated with particle-in-cell simulations [29,30]. Another laser (probe laser, neodymium-doped yttrium aluminum garnet) with energy of 330 mJ in 10 ns at a wavelength of 532 nm focused at the origin  $(x, y, z) = (0, 0, 0)$ , and the Thomson scattered light was detected from two directions (TS1 and TS2). The probe laser direction was  $45^\circ$  from  $x$  and  $z$  axes, and the axis  $p$  is defined along the probe laser:  $(x, y, z) = (p/\sqrt{2}, 0, -p/\sqrt{2})$ . LTS measures local plasma parameters along the probe laser, and the spatial resolution is determined by the focal spot,  $l_{\text{LTS}} \sim 100 \mu\text{m}$ , as shown in Fig. 4(d). The resolution in wavelength is determined by the entrance slit and the dispersion in the spectrometer, which is directly measured by observing Rayleigh scattering from nitrogen gas filled in the vacuum chamber. We used a high-wavelength-resolution spectrometer with triple-grating systems [7,9,31] and the resolutions were  $25 \pm 1 \text{ pm}$  for TS1 and  $20 \pm 1 \text{ pm}$  for TS2, and the dispersed light was detected with ICCD cameras with gate widths of 3 ns. The top view of this geometry is also illustrated in Fig. 4(b). These two diagnostics measure plasma parameters in two different directions ( $k_1$  and  $k_2$ ) as shown in Fig. 4(c). Plasma density structure was also imaged with an ICCD camera with gate width of 0.2 ns by observing a self-emission at the wavelength of  $450 \pm 5 \text{ nm}$ .

#### A. Self-emission imaging

Figures 5(a)–5(d) show the SE images taken from  $t = 4$ –9 ns. The dashed lines show the surface of the carbon target. Generally, the emission intensity is interpreted as thermal bremsstrahlung emission in optically thin plasma, and it strongly depends on the electron density [32]. Early in time at  $t = 4$ –5 ns [Figs. 5(a) and 5(b)], two plasmas begin to interact on the midplane,  $y = 0 \text{ mm}$ . Two planar structures are formed at  $y > 0 \text{ mm}$  and  $y < 0 \text{ mm}$  at  $t = 7 \text{ ns}$  as shown in Fig. 5(c). As the two plasmas with self-generated magnetic fields expand, antiparallel field structures would be piled up on the midplane [19,26,27,29,33], and the stronger field decelerates the plasma expansion, forming these dense structures as shown with dashed lines in the enlarged figure [Fig. 5(e)]. These dense structures begin to merge at  $z \sim 0$  at  $t = 7 \text{ ns}$ , and continue to merge at  $z > 0$  later in time forming a single planar structure as shown in Fig. 5(g). This indicates the plasma stagnation due to the decrease in magnetic pressure on the midplane.

#### B. LTS parallel to $B$

LTS spectra parallel to the  $k_1$  vector [see Fig. 4(c)] measured in the direction of TS1 at  $t = 5, 7,$  and  $9 \text{ ns}$  are shown in Figs. 6(a)–6(c), respectively. The observed two peaks show the ion feature, and the peak separation is proportional to the sound velocity:  $\omega/k \sim c_s \sim [(ZT_e + 3T_i)/m_i]^{1/2}$ . The widths of the spectra decrease from  $t = 5$  to  $9 \text{ ns}$ , suggesting that the temperature decreases in time. Small fluctuations in bulk-flow velocity are observed at  $t = 5$  and  $7 \text{ ns}$  around  $p \sim 0 \text{ mm}$  [dashed lines in Figs. 6(a) and 6(b)], and different widths in left and right peaks are seen as well. This difference is easily seen in the line-out plots shown in Figs. 6(d) and 6(e), at  $p = -0.15$  and  $0.25 \text{ mm}$ , respectively. The light intensity around  $\Delta\lambda \sim 0$  decreases by a notch filter as shown in

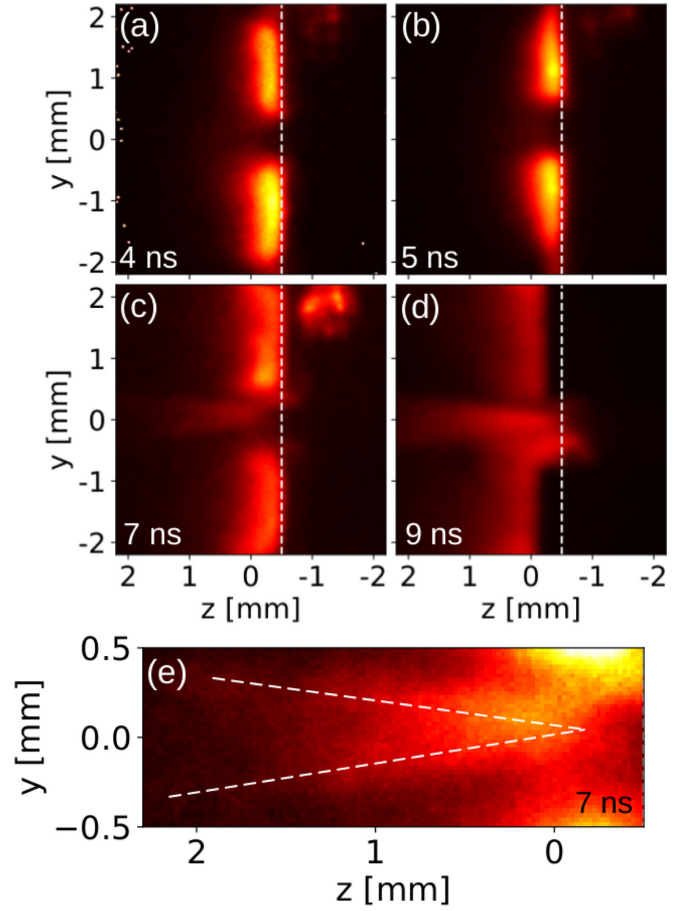


FIG. 5. SE images at (a)  $t = 4$ , (b)  $5$ , (c)  $7$ , and (d)  $9 \text{ ns}$ . (e) The enlarged figure of colliding plasmas at  $t = 7 \text{ ns}$  (c). Two plasmas expanding from the upper and lower targets slow down by the piled-up magnetic field near the plane  $y = 0$ , and dense structures are formed along the dashed lines.

the shaded areas. These spectra show different widths for the left and right peaks and this difference cannot be interpreted using Maxwellian distributions for electrons and ions, but explained with non-Maxwellian ion velocity distribution as explained in Sec. II C. Assuming the ion velocity distribution as a superposition of two Maxwellians, observed asymmetric features can be expressed. Here, a collisional-radiative model is assumed and the average charge state  $Z_i$  is evaluated as a function of  $T_e$  and  $n_e$ ,  $Z_i = Z_i(T_e, n_e)$ , using the FLYCHK code [34]. The solid lines are the best-fit results, and the dotted and dashed lines are the spectra calculated from Maxwellian ion velocity distributions. Here, we assume that the plasma is in the collisionless regime for LTS measurement; that is, the ion-ion mean free path for thermal ions,  $\lambda_i$ , is much larger than  $1/k$ , or  $k\lambda_i \gg 1$ , where  $k$  is the wave number of the ion acoustic wave [35]. For example,  $\lambda_i \sim 12\pi^2 \epsilon_0^2 (k_B T_i)^2 / \sqrt{\pi} Z^4 e^4 n_i \ln \Lambda = 4.3 \mu\text{m}$  [35], where  $\ln \Lambda \sim 6.2$  is the Coulomb logarithm, with the typical parameters of  $T_i = 300 \text{ eV}$ ,  $Z = 4$ , and  $n_i = 2.7 \times 10^{18} \text{ cm}^{-3}$ ,  $n_e = 1.7 \times 10^{19} \text{ cm}^{-3}$ , and  $k = k_1 = k_2 = 1.7 \times 10^7 \text{ m}^{-1}$ , resulting in  $k\lambda_i \sim 72$ , and the collisional effect is small in the present experiment.

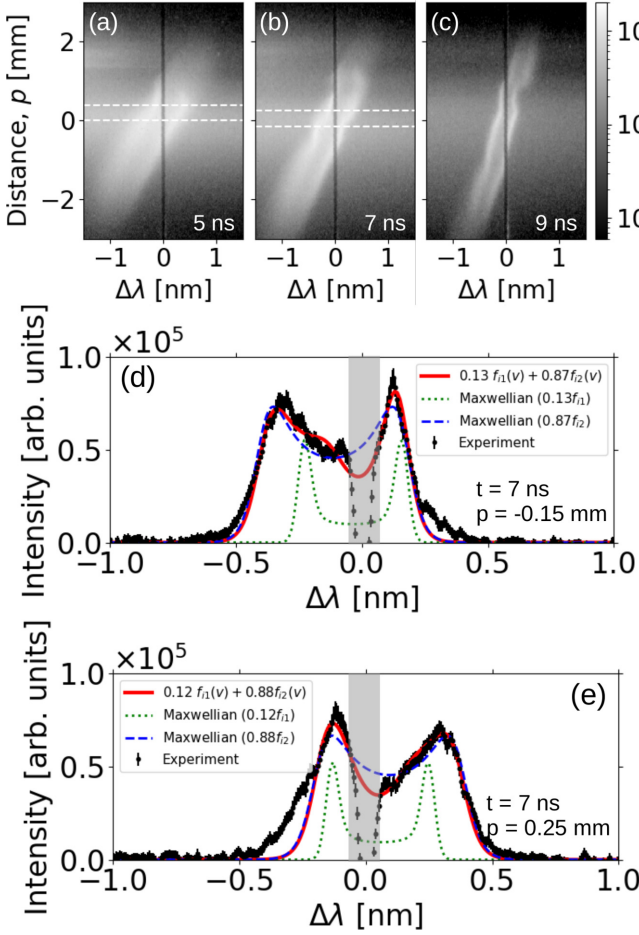


FIG. 6. LTS spectra along  $k_1$  at (a)  $t = 5$ , (b) 7, and (c) 9 ns. The line-out plots at  $t = 7$  ns at (d)  $p = -0.15$  mm and (e) 0.25 mm. These spectra are fitted with Eq. (16) and shown with solid lines. Theoretical functions with single Maxwellian distribution are shown with dotted ( $f_1$ ) and dashed ( $f_2$ ) lines. The shaded areas are affected by a notch filter or stray light.

The corresponding velocity distributions are shown in Figs. 7(a) and 7(b). The best-fit results (solid lines) show a non-Maxwellian distribution consisting of two ion distributions with different temperatures and drift velocities (dashed and dotted lines). When the ions drift in the  $k_1$  direction at  $p = -0.15$  mm [Fig. 6(d)], the observed spectrum is explained with  $0.13f_1 + 0.87f_2$ , where  $f_1$  and  $f_2$  are Maxwellian distributions with temperatures of  $69 \pm 4$  and  $290 \pm 5$  eV, respectively, and drift velocities of  $14 \pm 1$  and  $46 \pm 1$  km/s, respectively. On the other hand, ions drift in the  $-k_1$  direction at  $p = 0.25$  mm, and expressed with  $0.12f_1 + 0.88f_2$ , where  $f_1$  and  $f_2$  are Maxwellian distributions with  $T_i = 72 \pm 11$  eV and  $v_i = -23 \pm 2$  km/s, and  $T_i = 300 \pm 12$  eV and  $v_i = -37 \pm 1$  km/s, respectively.

The ion density, electron and ion temperatures, and flow velocity at  $t = 7$  ns as a function of position  $p$  are obtained from the fitting of the spectrum of Fig. 6(b) and shown in Fig. 8. The observed spectrum at  $-0.4 < p < 0.4$  mm are well fitted with two components with low-density and low-temperature ions (inverted triangles) and high-density and high-temperature ions (triangles) shown in Figs. 8(a) and 8(b).

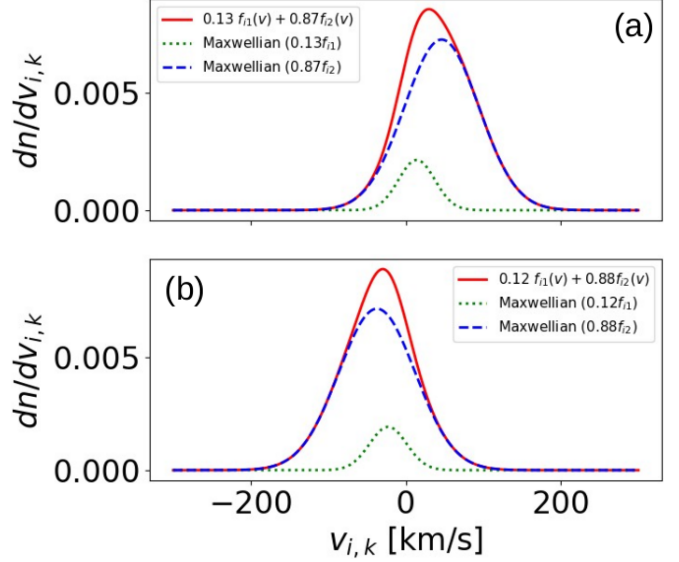


FIG. 7. Ion velocity distributions with the parameters obtained from the fitting of Figs. 6(d) and 6(e).

The electron temperatures [squares in Fig. 8(b)] are almost the same as the ion temperatures of the lower-temperature component. In addition, the lower-temperature ions show slower flow velocity and this flow velocity is comparable to a free-streaming velocity calculated as  $v = p/\sqrt{2t}$  as shown with dashed line in Fig. 8(c). On the other hand, the ion population with higher velocity and higher temperature are observed as shown with triangles in Fig. 8(c). This velocity shift from the free-streaming velocity ( $\Delta v \sim 30$  km/s) can be interpreted as an acceleration. These figures suggest that about 90% of the ions are thermalized and accelerated in the  $\pm k_1$  directions (or  $\pm x$  directions), which are consistent with the directions of outflows from a magnetic reconnection between the antiparallel self-generated Biermann battery fields.

We also performed a laser shot with only a single beam for plasma generation, and the ion density, temperatures, and flow velocity are shown with circles in Figs. 8(a)–8(c), respectively. The flow velocity in the case of a single laser shot is almost the same as the free-streaming velocity shown with a dashed line in Fig. 8(c), and similar to the slower ion component (inverted triangles). Therefore, the slower (lower-temperature) ion component is considered as the plasma directly expands from the laser spot, while the faster (higher-temperature) plasma is interpreted as the outflow energized by a magnetic reconnection.

### C. LTS perpendicular to $B$

Figures 9(a)–9(d) show LTS spectra along  $k_2$  (perpendicular to the initial antiparallel magnetic field  $B$ ) at  $t = 5, 6, 7$ , and 9 ns, respectively. Unlike the spectra in the  $k_1$  direction (see Fig. 6), the spectra are almost straight as a function of position  $p$  with constant width, meaning there is no characteristic change in velocity or temperature.

Figures 10(a)–10(d) show the line-outs of Figs. 9(a)–9(d) at  $p = -0.3$  mm at  $t = 5, 6, 7$ , and 9 ns, respectively. The right peaks are stronger than the left peaks from  $t = 5$  to 7 ns.

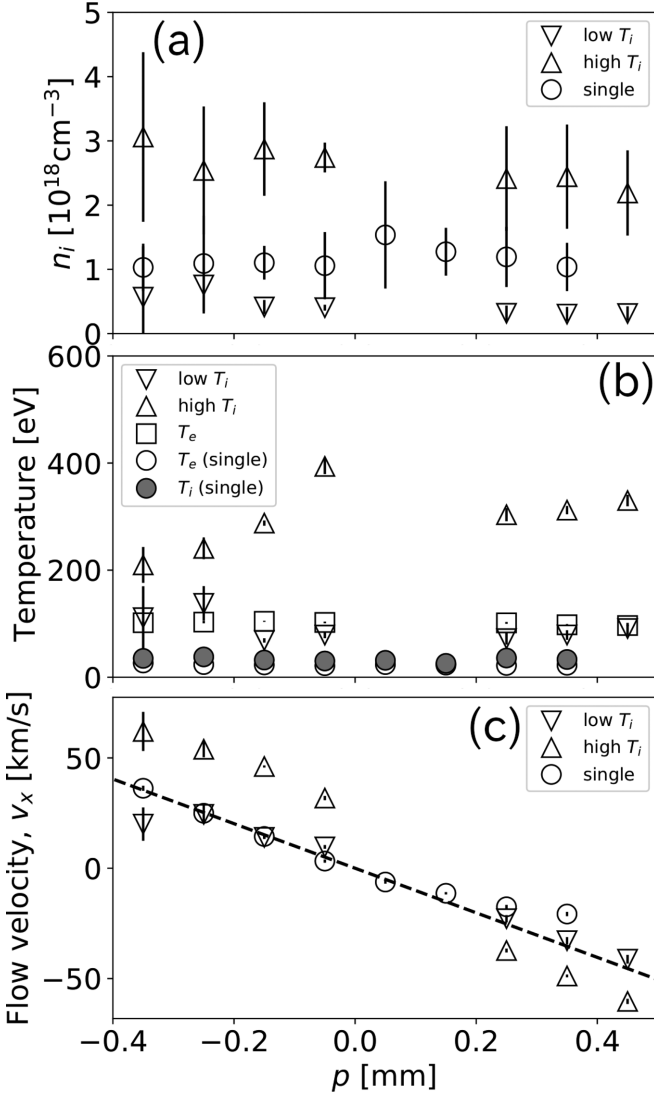


FIG. 8. (a) Ion density, (b) electron and ion temperatures, and (c) flow velocities obtained from the fitting of LTS spectra at  $t = 7$  ns. The plasma parameters obtained from a single laser shot are also shown with circles. The velocity calculated from the distance  $p$  and time  $t$ ,  $v = p/\sqrt{2}t$ , is plotted as a reference for free-streaming velocity.

However, the asymmetry is getting weaker as time evolves, and at 9 ns, the double peak becomes almost symmetric. This asymmetry is often interpreted as the different Landau damping on the ion acoustic waves in the  $\pm k_z$  directions (Sec. II B). When the ions and electrons are in Maxwellian velocity distribution, this difference occurs with different drift velocities of electron and ion flows. The solid lines show the results of fitting assuming Maxwellian distributions for both ions and electrons, resulting in  $T_e \sim 96, 77, 68,$  and  $45$  eV,  $T_i \sim 390, 310, 200,$  and  $220$  eV,  $v_{ei} \sim 650, 430, 270,$  and  $100$  km/s,  $n_e \sim 2.1 \times 10^{19}, 1.3 \times 10^{19}, 9.9 \times 10^{18},$  and  $1.3 \times 10^{19} \text{ cm}^{-3}$ , and, therefore, the estimated current density,  $j_z = Zen_i v_i - en_e v_e \sim 1.9 \times 10^{12}, 9.2 \times 10^{11}, 4.4 \times 10^{11},$  and  $8.7 \times 10^{10} \text{ A m}^{-2}$ , respectively, at  $t = 5, 6, 7,$  and  $9$  ns. Figure 11 shows the current density,  $j_z$ , as a function of position  $p$  at  $t = 5, 6, 7,$  and  $9$  ns, where we assume both electrons

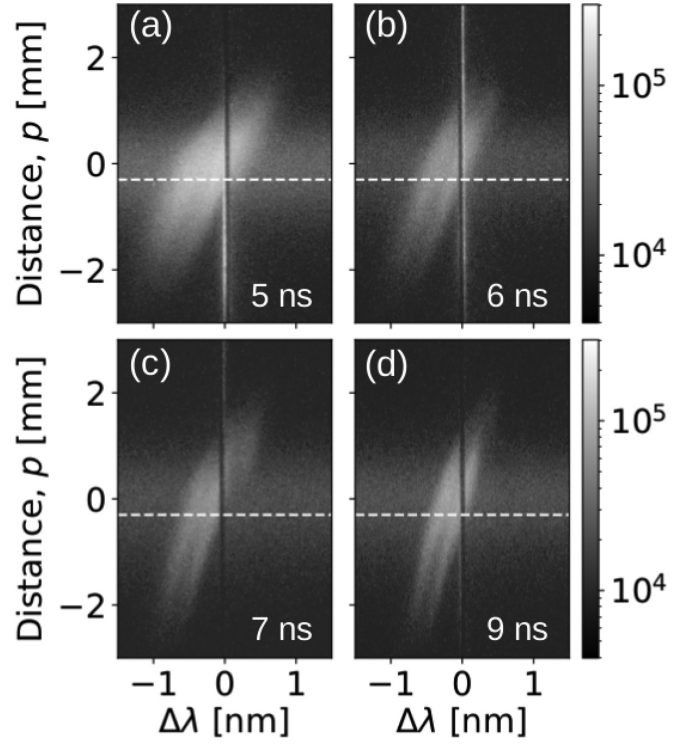


FIG. 9. LTS spectra with  $k \perp B$  at (a)  $t = 5$ , (b)  $6$ , (c)  $7$ , and (d)  $9$  ns.

and ions are in Maxwellian distribution. Although the spectra are affected by a notch filter at  $\Delta\lambda \sim 0$  and those at  $p > 0$  could not be analyzed, the current is detected in the region  $-0.5 < p < 0$  mm, suggesting the antiparallel field structure formation near  $y \sim 0$ .  $j_z \sim 2 \times 10^{12} \text{ A m}^{-2}$  at  $t = 5$  ns is the largest, and it decreases and almost disappears at  $t = 9$  ns.

#### IV. DISCUSSION

As previously reported in many researches with laser-produced plasmas [19,26,27,29,33], a stable magnetic-field structure with antiparallel directions is formed between two laser-produced plasma plumes as shown in Figs. 4(a), 4(d), and 12. In such a field structure, an electron current would be generated in an electron dissipation region (EDR) satisfying

$$\int_{S_1} \mu_0 j_z \cdot dS_1 = \int_{S_1} (\nabla \times \mathbf{B}) \cdot dS_1 = \oint_{\delta S_1} \mathbf{B} \cdot d\mathbf{l}, \quad (20)$$

where  $j_z$  is the electron current and  $S_1$  is the cross section of the current sheet. This current  $j_z$  flows perpendicular to the plane on the antiparallel magnetic field ( $+z$  or  $+k_z$  direction in Figs. 4 and 12). Taking the thickness of the current sheet as  $\delta_e$ , the magnetic-field strength  $B_{in}$  in the upstream region is

$$B_{in} \sim \frac{\mu_0}{2} \delta_e j_z. \quad (21)$$

In general, the thickness of meandering charged particles is estimated as  $d \sim \sqrt{r_c \lambda_B}$ , where  $r_c$  is the Larmor radius for the magnetic field of  $B_{in}$ , assuming the magnetic-field strength  $B_x(y) = -B_{in}y/\lambda_B$  in a plasma sheet [36]. Here, the magnetic field varies in  $\lambda_B$  which is comparable to an ion diffusion region (IDR),  $\delta$ , where ions are unmagnetized and electrons are still magnetized. This thickness  $\delta$  ( $\sim \lambda_B$ ) should

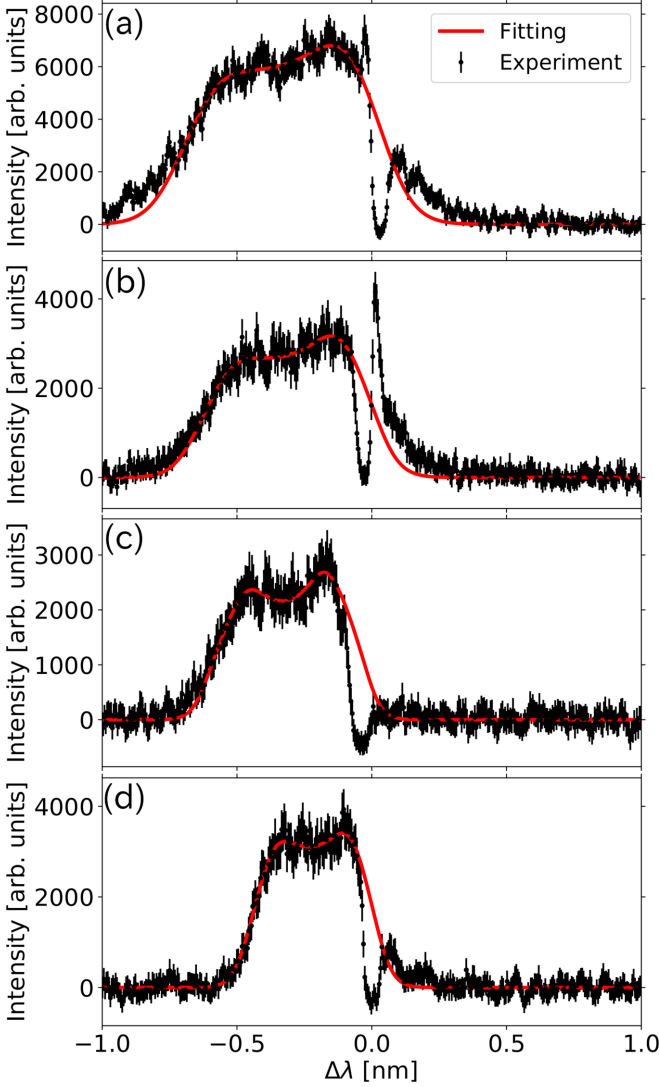


FIG. 10. LTS spectra at  $p = -0.3$  mm with  $k \perp \mathbf{B}$  at (a)  $t = 5$ , (b) 6, (c) 7, and (d) 9 ns.

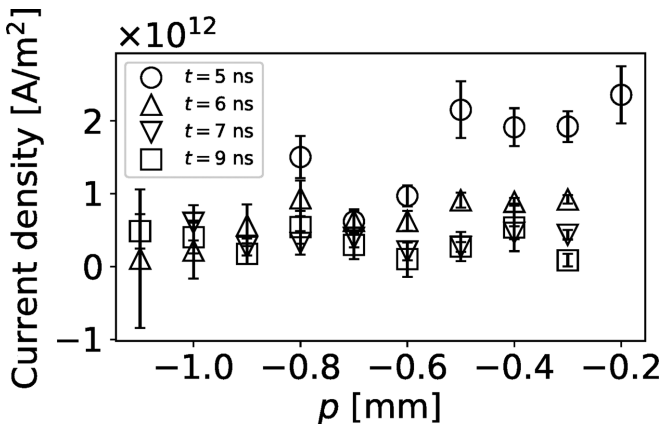


FIG. 11. The current density calculated at  $t = 5, 6, 7,$  and  $9$  ns as a function of position  $p$ , assuming that electrons and ions are in Maxwellian velocity distributions.

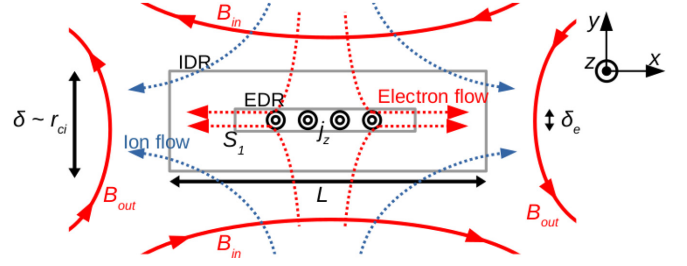


FIG. 12. Structure of the magnetic reconnection layer. Ions are magnetized outside of the IDR (the region  $L \times \delta$ ) and electrons are still magnetized. Electron current is formed and magnetic field diffuses in the EDR (in the thickness of  $\delta_e$ ).

be comparable to ion meandering thickness  $d$ , and, therefore,  $d \sim r_{ci} \sim \delta \sim \lambda_B$ . For electrons, the thickness of electron meandering or that of the electron current sheet is

$$\delta_e \sim \sqrt{r_{ce}\lambda_B} \sim \sqrt{r_{ce}r_{ci}}. \quad (22)$$

As shown in Figs. 10(a)–10(d), the electrons drift relative to ions from  $t = 5$  to  $9$  ns in the  $k_2$  direction, suggesting the electron current formation in the antiparallel magnetic field. Also this asymmetry decreases at  $t = 9$  ns, meaning the disappearance of this electron current. However, as explained in Sec. II B, this asymmetric spectrum can be expressed not only by Maxwellian electrons and ions with different flow velocities but also by non-Maxwellian electron velocity distribution with different Landau damping rates on the ion acoustic waves in the  $\pm k_2$  directions, indicating that the electron flow velocity and current density are not constrained only from this asymmetric ion feature. Therefore, we estimate  $j_z$  and  $B_{in}$  not from TS2 ( $k_2$  or  $z$  direction) but from TS1 ( $k_1$  or  $x$  direction), assuming that the acceleration in the  $\pm x$  directions is caused by magnetic reconnection and the outflow velocity is determined by the Alfvén velocity.

Here, considering the conservations of mass and energy during a magnetic reconnection,

$$\rho_{in}Lv_{in} = \rho_{out}\delta v_{out}, \quad (23)$$

$$(S_{in} + K_{in} + H_{in})v_{in}L = (S_{out} + K_{out} + H_{out})v_{out}\delta, \quad (24)$$

where  $Sv = (B^2/\mu_0)v$  is Poynting flux,  $Kv = (\rho v^2/2)v$  and  $Hv = (u + p)v$  are kinetic and enthalpy fluxes, respectively,  $\rho = m_i n_i$  is the mass density,  $u = p/(\gamma - 1)$  is the internal energy,  $p = nT$ , and  $L$  and  $\delta$  represent the length and width of the IDR shown in Fig. 12 with the thickness of  $\delta \sim r_{ci}$ . As suggested in Figs. 8(b) and 8(c), the kinetic energy is  $K_{out}/n_i \sim m_i v_{out}^2/2 \sim 60$  eV using the accelerated velocity of  $\sim 30$  km/s, while the internal energy is  $u_{out}/n_i \sim 300/(\gamma - 1)$  eV, indicating  $u_{out} \sim 5K_{out}/(\gamma - 1)$ . When the Poynting flux and kinetic energy density flux of the inflow are converted to the kinetic and enthalpy fluxes in the outflow (assuming  $H_{in} = S_{out} = 0$ ), the energy equation becomes

$$\left( \frac{B_{in}^2}{\mu_0} + \frac{\rho_{in}v_{in}^2}{2} \right) Lv_{in} \sim \frac{6\gamma - 1}{\gamma - 1} K_{out}\delta v_{out}. \quad (25)$$



By using Eq. (23) and assuming  $\gamma = 5/3$ ,

$$\begin{aligned} v_{\text{out}} &\sim \sqrt{\frac{2(\gamma-1)}{6\gamma-1}} \sqrt{\frac{B_{\text{in}}^2}{\mu_0 \rho_{\text{in}}} + \frac{v_{\text{in}}^2}{2}} \\ &\sim 0.38 \sqrt{v_A^2 + \frac{v_{\text{in}}^2}{2}}. \end{aligned} \quad (26)$$

Here,  $v_A$  is the Alfvén velocity defined by  $B_{\text{in}}$  and  $\rho_{\text{in}}$  in the upstream region. As observed in the SE image at  $t = 7$  ns [Fig. 5(c)], the inflow plasmas stagnate near the midplane, suggesting  $v_{\text{in}} \sim 0$  and  $K_{\text{in}} \sim 0$ . Therefore, Eq. (26) becomes

$$v_{\text{out}} \sim 0.38 v_A. \quad (27)$$

The acceleration of ion flows observed at  $t = 7$  ns shown in Figs. 7 and 8(c) can be interpreted as the outflows accelerated by magnetic reconnection. Using  $v_{\text{out}} = 30$  km/s ( $v_A = 78$  km/s),  $n_i \sim 1.5 \times 10^{18}$  cm $^{-3}$  (half of the measured ion density),  $T_e \sim 70$  eV,  $T_i \sim 100$  eV, and  $Z \sim 5.6$  for the lower-temperature component (Fig. 8), and Eqs. (21), (22), and (27),  $B_{\text{in}} \sim 15$  T,  $\delta_e \sim 11$   $\mu\text{m}$ , and  $j_z \sim 2.2 \times 10^{12}$  A m $^{-2}$ . The current is roughly consistent with other previous measurements with proton radiography. For example, in the experiment at the National Ignition Facility (NIF) [37], path-integrated peak current density was estimated as  $\int j_z dl \sim 1.6 \times 10^8$  A m $^{-1}$  or  $1.6 \times 10^{11}$  A m $^{-2}$  with a measured magnetic field of  $B_{\text{in}} \sim 5$  T assuming the integrated length of 1 mm, averaged in the thickness of 58  $\mu\text{m}$ , which is comparable to the present result,  $2.2 \times 10^{12}$  A m $^{-2}$  in the electron current sheet of 11  $\mu\text{m}$  or  $\sim 2.4 \times 10^{11}$  A m $^{-2}$  averaged in the measurement region of  $\sim 100$   $\mu\text{m}$ . The magnetic-field diffusion rate in the current sheet or reconnection rate is the rate of the field flux change in the upstream region:

$$R = \frac{1}{v_A B_{\text{in}}} \left| \frac{d\Phi_{\text{in}}}{dt} \right|, \quad (28)$$

where the rate is normalized by  $v_A B_{\text{in}}$ ,  $\Phi_{\text{in}}$  is the magnetic-field flux in the upstream region  $\Phi_{\text{in}} = \int B_x dy$  in the  $xy$  plane assuming  $\partial B_x / \partial z = 0$ , and is roughly  $\Phi_{\text{in}} \sim B_{\text{in}} \lambda_B / 2$  assuming  $B_x(y) \sim -B_{\text{in}}(y/\lambda_B)$  in the plasma sheet, and  $B_{\text{in}} \sim 15$  T is estimated at  $t = 7$  ns. The asymmetric spectra, suggesting the ion flow acceleration, appears at  $t = 5$ – $7$  ns (see Figs. 6 and 8) and the current disappears at  $t = 9$  ns (see Fig. 11). Although  $\lambda_B$  and  $B_{\text{in}}$  change during the magnetic reconnection and we have no magnetic field measurement here, we assume  $\lambda_B \sim r_{\text{ci}} \sim 60$   $\mu\text{m}$  and total flux,  $\Phi_{\text{in}}$ , disappears in  $\Delta t \sim 4$  ns (5–9 ns). Therefore, the reconnection rate becomes  $R \sim 0.096$ , which is comparable to the universal reconnection rate of 0.1 for Hall magnetic reconnection where the rate is determined only by local plasma parameters [1,38,39]. However, the rate would be precisely determined by measuring a spatial distribution of  $B_{\text{in}}$  and  $\lambda_B$  by proton radiography technique [6,27,37] in addition to multidirectional LTS measurements in future experiments. Though  $B_{\text{in}}$  is estimated only at  $t = 7$  ns in the present experiment, the time evolution of the rate would also be determined by measuring the time evolution of LTS spectra in both directions with better time resolution or with a streak camera instead of ICCD camera.

For the estimation of plasma parameters in the  $k_1$  direction,  $\sim 87\%$  of the ions are the high-temperature component while only  $\sim 13\%$  are the low-temperature component, i.e.,  $\rho_{\text{hot}}/\rho_{\text{cold}} = 0.87/0.13 = 6.7$ , where  $\rho_{\text{hot}}$  and  $\rho_{\text{cold}}$  are the densities of the high- and low-temperature components, respectively. Here, the high-temperature component is considered as the outflow from magnetic reconnection,

$$\rho_{\text{hot}} \sim \rho_{\text{out}}, \quad (29)$$

while the low-temperature component is the plasma coming from the two laser spots directly. However, as shown in Fig. 8(a), the density of the low-temperature component is smaller than that of the single flow, i.e.,  $\rho_{\text{cold}} < \rho_{\text{single}}$ . In addition,  $\rho_{\text{in}}$  should be larger than  $\rho_{\text{single}}$  because of the deceleration of the inflows as observed in SE images, resulting in

$$\rho_{\text{in}} > \rho_{\text{single}} > \rho_{\text{cold}} = r \rho_{\text{in}} \quad (0 < r < 1). \quad (30)$$

From the conservations of magnetic-field flux and mass,

$$\frac{\rho_{\text{out}}}{\rho_{\text{in}}} = \frac{v_{\text{in}} L}{v_{\text{out}} \delta} \sim R \frac{L}{\delta}, \quad (31)$$

where  $R = v_{\text{in}}/v_{\text{out}} = B_{\text{out}}/B_{\text{in}}$  is the reconnection rate which is already estimated as  $R \sim 0.1$ . The length  $L$  is, generally, larger than  $\delta$ , and we observed bidirectional flows separated by  $\sim 400$   $\mu\text{m}$  along the  $p$  axis [see Fig. 8(b)] indicating  $\sim 300$   $\mu\text{m}$  along the  $x$  axis, and roughly  $L \sim 300$   $\mu\text{m}$ , while  $\delta \sim 60$   $\mu\text{m}$ . Therefore, using Eqs. (29)–(31), we get

$$\frac{\rho_{\text{hot}}}{\rho_{\text{cold}}} = \frac{\rho_{\text{out}}}{r \rho_{\text{in}}} \sim \frac{RL}{r\delta} \sim 0.5/r, \quad (32)$$

and the observed ratio  $\rho_{\text{hot}}/\rho_{\text{cold}} = 6.7$  is explained with small  $\rho_{\text{cold}}$  relative to  $\rho_{\text{in}}$  or small  $r \sim 0.075$ .

Here, the ion and electron Larmor radii are estimated as  $r_{\text{ci}} \sim 60$   $\mu\text{m}$  and  $r_{\text{ce}} \sim 1.9$   $\mu\text{m}$ , respectively, at  $t = 7$  ns (using  $T_i = 100$  eV,  $T_e = 70$  eV,  $Z_i = 5.6$ , and  $B = 15$  T) and both are smaller than the typical system size  $l_{\text{typ}} \sim 1$  mm. In addition, the spatial resolution of the LTS is roughly  $l_{\text{LTS}} \sim 100$   $\mu\text{m}$  [see LTS volume in Fig. 4(d)], and  $r_{\text{ce}} \ll r_{\text{ci}} \lesssim l_{\text{LTS}} \ll l_{\text{typ}}$ , meaning that both electrons and ions are magnetized in the ablation plasma, and electrons are still magnetized in the LTS measurement volume. As previously reported [6], the laser-produced plasma has large  $T_e$  ( $\sim 1$  keV) and  $n_e$  ( $\sim 10^{20-22}$  cm $^{-3}$ ) early in time around the laser spot, and strong magnetic field of  $B \sim 100$  T is formed via the Biermann battery effect, resulting in large plasma  $\beta$ ,  $\beta_e = 2\mu_0 n_e T_e / B^2 \sim 4$ – $400$ . It becomes small, for example, at  $t \sim 7$  ns,  $\beta_e \sim 1.3$ . The Lundquist number at  $t \sim 7$  ns is estimated as  $S = Lv_A / D_M \sim 270$ , where  $L$  is the system size of  $\sim 1$  mm,  $v_A = B_{\text{in}} / \sqrt{\mu_0 \rho_{\text{in}}} \sim 78$  km/s in the upstream region,  $D_M = v_{ei}(c/\omega_{pe})^2 \sim 0.29$  m $^2$ s $^{-1}$  is the magnetic diffusivity, and  $v_{ei} = 1.2 \times 10^{11}$  s $^{-1}$  is electron-ion collision frequency [40] with  $n_e \sim 1.7 \times 10^{19}$  cm $^{-3}$  and  $T_e \sim 70$  eV. Previous numerical simulations [41–43] have suggested that the current sheet becomes stochastic at high Lundquist number such as  $S > 10^4$  due to tearing instability, but is in quasisteady state in relatively small  $S$  ( $< 10^4$ ) which is in our experimental condition.

The spectra parallel to  $B_{\text{in}}$  (Fig. 6) show sharp peaks suggesting ion acoustic resonance. On the other hand, the spectra perpendicular to  $B_{\text{in}}$  (Fig. 10) show weak resonance suggesting strong damping of ion acoustic waves with  $T_i > T_e$ . These differences in spectra are explained with nonequal temperature in two directions,  $T_{i\perp} \neq T_{i\parallel}$  and/or  $T_{e\perp} \neq T_{e\parallel}$ , where  $\parallel$  and  $\perp$  represent the directions relative to  $B_{\text{in}}$ , respectively. This anisotropy in velocity distribution may come from Speiser orbits and meandering motions around the diffusion region and has been observed by the Magnetospheric Multiscale Mission (MMS) [44] and numerical simulations [45], and can be further investigated in future experiments in the method presented here.

In the present experiment, the Biermann battery fields are advected with expanding plasmas and the antiparallel field structure is formed in the  $x$  direction near the plane  $y = 0$  and the reconnection can occur anywhere in the  $z$  axis. As the SE imaging shows, two plasmas from the top and bottom interact with each other at  $z \sim 0$ , while the antiparallel field structure still exists at  $z \gtrsim 0$  at  $t = 7$  ns. This indicates that the magnetic pressure decreases at  $z \sim 0$  due to magnetic-field diffusion in the current sheet. The electron current is measured from  $t = 5$  to 9 ns in the  $z$  direction, accompanied by the bipolar ion flows accelerated in the  $\pm x$  directions at  $t = 5$  and 7 ns. These measurements suggest that the antiparallel Biermann fields reconnect in the electron current sheet at  $(x, y, z) \sim (0, 0, 0)$ , accelerating the plasma as outflows during  $t \sim 5\text{--}9$  ns, and it ends at  $t \gtrsim 9$  ns.

## V. SUMMARY

We have measured the appearance and disappearance of an electron current sheet as well as bidirectional ion flows in the magnetic reconnection between laser-produced magnetized plasmas. We have investigated the magnetic reconnection and magnetic diffusion region formed in a self-generated antiparallel magnetic field by using optical diagnostics: Two-directional laser Thomson scattering and self-emission imaging. Thomson scattering spectra perpendicular to the magnetic field show different Landau damping effects on ion acoustic waves in the  $\pm z$  directions, indicating the current-sheet formation. The spectra parallel to the magnetic field show different widths in two peaks, which are interpreted as non-Maxwellian ion velocity distribution and two different components: Cold and slow ions and hot and faster ions. This acceleration along the magnetic field is explained as the outflow from the magnetic reconnection. Assuming that the additional velocity is comparable to the Alfvén velocity

defined with the upstream plasma parameters, the magnetic field in the upstream region is  $B_{\text{in}} \sim 15$  T. The current density in the electron current sheet,  $j_z \sim 2.2 \times 10^{12}$  A m $^{-2}$ , is nearly consistent with that obtained from the spectra obtained in the perpendicular direction,  $j_z \sim (0.4\text{--}1.9) \times 10^{12}$  A m $^{-2}$ , and is also comparable to the estimation from proton radiography of similar laser experiments. Combining two directional data, the current is formed from  $t \sim 5$  to 9 ns accompanied by bidirectional plasma flows observed at  $t \sim 7$  ns due to magnetic reconnection. The SE imaging shows the stagnation of two plasmas showing two separated dense regions. These structures interact and merge at  $t > 7$  ns, which can be interpreted as the magnetic pressure decrease due to magnetic reconnection. While the electron current is detected here, both electron and ion velocity distributions are needed to directly measure the current sheet. These can be measured with noncollective LTS for smaller density or shorter wavelength for the probe laser, or the electron velocity distribution at the phase velocity of electron plasma waves can be obtained from the electron feature of collective LTS in future experiments. Also, multiple-direction LTS can reveal asymmetric ion velocity distributions in  $x$ ,  $y$ , and  $z$  directions resulting from Speiser orbits and meandering motions in the outflow region, which has been analyzed and discussed by using particle-in-cell simulations [45] and by MMS observation [44].

The magnetic reconnection rate is estimated as  $R \sim 0.1$  assuming a spatial distribution of  $B_{\text{in}}(y)$  averaged in 5–9 ns. This reconnection rate can be estimated precisely by using LTS presented here and by using magnetic field measurement, for example, proton radiography, simultaneously in future experiments.

## ACKNOWLEDGMENTS

The authors would like to acknowledge the dedicated technical support of the staff at the Gekko-XII facility for the laser operation, target fabrication, and plasma diagnostics. We would also like to thank N. Ozaki for the target alignment in the experiment, and M. Hoshino, S. Zenitani, Y. Ohira, and N. Yamamoto for helpful comments and valuable discussions. This research was partially supported by JSPS KAKENHI Grants No. JP22H01251, No. JP22H00119, No. JP20H01881, No. JP20K20285, No. JP18H01232, and No. JP17H06202, JSPS Core-to-Core Program B:Asia- Africa Science Platforms Grant No. JPJSCCB20190003, and by the joint research project of the Institute of Laser Engineering, Osaka University.

[1] M. Yamada, R. Kulsrud, and H. Ji, *Rev. Mod. Phys.* **82**, 603 (2010).  
 [2] E. G. Zweibel and M. Yamada, *Annu. Rev. Astron. Astrophys.* **47**, 291 (2009).  
 [3] M. J. Rosenberg, C. K. Li, W. Fox, A. B. Zylstra, C. Stoeckl, F. H. Séguin, J. A. Frenje, and R. D. Petrasso, *Phys. Rev. Lett.* **114**, 205004 (2015).

[4] J. Zhong, Y. Li, X. Wang, J. Wang, Q. Dong, C. Xiao, S. Wang, X. Liu, L. Zhang, L. An, F. Wang, J. Zhu, Y. Gu, X. He, G. Zhao, and J. Zhang, *Nat. Phys.* **6**, 984 (2010).  
 [5] P. M. Nilson, L. Willingale, M. C. Kaluza, C. Kamperidis, S. Minardi, M. S. Wei, P. Fernandes, M. Notley, S. Bandyopadhyay, M. Sherlock, R. J. Kingham, M. Tatarakis, Z. Najmudin, W. Rozmus, R. G. Evans, M. G. Haines, A. E.

- Dangor, and K. Krushelnick, *Phys. Rev. Lett.* **97**, 255001 (2006).
- [6] C. K. Li, F. H. Séguin, J. A. Frenje, J. R. Rygg, R. D. Petrasso, R. P. J. Town, O. L. Landen, J. P. Knauer, and V. A. Smalyuk, *Phys. Rev. Lett.* **99**, 055001 (2007).
- [7] R. Yamazaki, S. Matsukiyo, T. Morita, S. J. Tanaka, T. Umeda, K. Aihara, M. Edamoto, S. Egashira, R. Hatsuyama, T. Higuchi, T. Hihara, Y. Horie, M. Hoshino, A. Ishii, N. Ishizaka, Y. Itadani, T. Izumi, S. Kambayashi, S. Kakuchi, N. Katsuki *et al.*, *Phys. Rev. E* **105**, 025203 (2022).
- [8] T. Morita, K. Tomita, K. Sakai, M. Takagi, K. Aihara, M. Edamoto, S. Egashira, T. Higuchi, N. Ishizaka, T. Izumi, S. Kakuchi, T. Kojima, Y. Kuramitsu, S. Matsukiyo, Y. Nakagawa, T. Minami, H. Murakami, Y. Nishioka, M. Ota, T. Sano *et al.*, *High Energy Density Phys.* **36**, 100754 (2020).
- [9] T. Morita, K. Nagashima, M. Edamoto, K. Tomita, T. Sano, Y. Itadani, R. Kumar, M. Ota, S. Egashira, R. Yamazaki, S. J. J. Tanaka, S. Tomita, S. Tomiya, H. Toda, I. Miyata, S. Kakuchi, S. Sei, N. Ishizaka, S. Matsukiyo, Y. Kuramitsu *et al.*, *Phys. Plasmas* **26**, 090702 (2019).
- [10] D. Froula, S. H. Glenzer, N. C. Luhmann, Jr., and J. Sheffield, *Plasma Scattering of Electromagnetic Radiation: Theory and Measurement Techniques* (Academic Press, New York, 2010), Vol. 2010.
- [11] J. S. Ross, S. H. Glenzer, P. Amendt, R. Berger, L. Divol, N. L. Kugland, O. L. Landen, C. Plechaty, B. Remington, D. Ryutov, W. Rozmus, D. H. Froula, G. Fiksel, C. Sorce, Y. Kuramitsu, T. Morita, Y. Sakawa, H. Takabe, R. P. Drake, M. Grosskopf *et al.*, *Phys. Plasmas* **19**, 056501 (2012).
- [12] G. F. Swadling, C. Bruulsema, F. Fiuza, D. P. Higginson, C. M. Huntington, H. S. Park, B. B. Pollock, W. Rozmus, H. G. Rinderknecht, J. Katz, A. Birkel, and J. S. Ross, *Phys. Rev. Lett.* **124**, 215001 (2020).
- [13] K. Sakai, T. Nishimoto, S. Isayama, S. Matsukiyo, and Y. Kuramitsu [arXiv:2210.11086](https://arxiv.org/abs/2210.11086).
- [14] J. S. Ross, H. S. Park, R. Berger, L. Divol, N. L. Kugland, W. Rozmus, D. Ryutov, and S. H. Glenzer, *Phys. Rev. Lett.* **110**, 145005 (2013).
- [15] H. S. Park, D. D. Ryutov, J. S. Ross, N. L. Kugland, S. H. Glenzer, C. Plechaty, S. M. Pollaine, B. A. Remington, A. Spitkovsky, L. Gargate, G. Gregori, A. Bell, C. Murphy, Y. Sakawa, Y. Kuramitsu, T. Morita, H. Takabe, D. H. Froula, G. Fiksel, F. Miniati *et al.*, *High Energy Density Phys.* **8**, 38 (2012).
- [16] Y. Sakawa, T. Ide, T. Morita, K. Tomita, K. Uchino, Y. Kuramitsu, N. Ohnishi, and H. Takabe, *High Energy Density Phys.* **23**, 207 (2017).
- [17] N. L. Kugland, D. D. Ryutov, P. Y. Chang, R. P. Drake, G. Fiksel, D. H. Froula, S. H. Glenzer, G. Gregori, M. Grosskopf, M. Koenig, Y. Kuramitsu, C. Kuranz, M. C. Levy, E. Liang, J. Meinecke, F. Miniati, T. Morita, A. Pelka, C. Plechaty, R. Presura *et al.*, *Nat. Phys.* **8**, 809 (2012).
- [18] F. Fiuza, G. F. Swadling, A. Grassi, H. G. Rinderknecht, D. P. Higginson, D. D. Ryutov, C. Bruulsema, R. P. Drake, S. Funk, S. Glenzer, G. Gregori, C. K. Li, B. B. Pollock, B. A. Remington, J. S. Ross, W. Rozmus, Y. Sakawa, A. Spitkovsky, S. Wilks, and H. S. Park, *Nat. Phys.* **16**, 916 (2020).
- [19] C. K. Li, V. T. Tikhonchuk, Q. Moreno, H. Sio, E. D'Humières, X. Ribeyre, P. Korneev, S. Atzeni, R. Betti, A. Birkel, E. M. Campbell, R. K. Follett, J. A. Frenje, S. X. Hu, M. Koenig, Y. Sakawa, T. C. Sangster, F. H. Séguin, H. Takabe, S. Zhang *et al.*, *Phys. Rev. Lett.* **123**, 055002 (2019).
- [20] D. B. Schaeffer, W. Fox, R. K. Follett, G. Fiksel, C. K. Li, J. Matteucci, A. Bhattacharjee, and K. Germaschewski, *Phys. Rev. Lett.* **122**, 245001 (2019).
- [21] D. B. Schaeffer, W. Fox, D. Haberberger, G. Fiksel, A. Bhattacharjee, D. H. Barnak, S. X. Hu, and K. Germaschewski, *Phys. Rev. Lett.* **119**, 025001 (2017).
- [22] S. R. Titorica, M. Hoshino, T. Abel, and F. Fiuza, *Phys. Plasmas* **27**, 112111 (2020).
- [23] J. Zhong, X. Yuan, B. Han, W. Sun, and Y. Ping, *High Power Laser Sci. Eng.* **6**, e48 (2018).
- [24] A. E. Raymond, C. F. Dong, A. McKelvey, C. Zulick, N. Alexander, A. Bhattacharjee, P. T. Campbell, H. Chen, V. Chvykov, E. Del Rio, P. Fitzsimmons, W. Fox, B. Hou, A. Maksimchuk, C. Mileham, J. Nees, P. M. Nilson, C. Stoeckl, A. G. R. Thomas, M. S. Wei *et al.*, *Phys. Rev. E* **98**, 043207 (2018).
- [25] J. A. Stamper and B. H. Ripin, *Phys. Rev. Lett.* **34**, 138 (1975).
- [26] P. M. Nilson, L. Willingale, M. C. Kaluza, C. Kamperidis, S. Minardi, M. S. Wei, P. Fernandes, M. Notley, S. Bandyopadhyay, M. Sherlock, R. J. Kingham, M. Tatarakis, Z. Najmudin, W. Rozmus, R. G. Evans, M. G. Haines, A. E. Dangor, and K. Krushelnick, *Phys. Plasmas* **15**, 092701 (2008).
- [27] W. Fox, A. Bhattacharjee, and K. Germaschewski, *Phys. Plasmas* **19**, 056309 (2012).
- [28] M. J. Rosenberg, C. K. Li, W. Fox, I. Igumenshchev, F. H. Séguin, R. P. J. Town, J. A. Frenje, C. Stoeckl, V. Glebov, and R. D. Petrasso, *Nat. Commun.* **6**, 6190 (2015).
- [29] J. Matteucci, W. Fox, A. Bhattacharjee, D. B. Schaeffer, C. Moissard, K. Germaschewski, G. Fiksel, and S. X. Hu, *Phys. Rev. Lett.* **121**, 095001 (2018).
- [30] W. Fox, J. Matteucci, C. Moissard, D. B. Schaeffer, A. Bhattacharjee, K. Germaschewski, and S. X. Hu, *Phys. Plasmas* **25**, 102106 (2018).
- [31] K. Tomita, Y. Sato, S. Tsukiyama, T. Eguchi, K. Uchino, K. Kouge, H. Tomuro, T. Yanagida, Y. Wada, M. Kunishima, G. Soumagne, T. Kodama, H. Mizoguchi, A. Sunahara, and K. Nishihara, *Sci. Rep.* **7**, 12328 (2017).
- [32] G. B. Rybicki and A. P. Lightman, *Radiative Processes in Astrophysics* (Wiley-VCH, Weinheim, Germany, 1980), Vol. 31, pp. 359–359.
- [33] C. K. Li, P. Tzeferacos, D. Lamb, G. Gregori, P. A. Norreys, M. J. Rosenberg, R. K. Follett, D. H. Froula, M. Koenig, F. H. Séguin, J. A. Frenje, H. G. Rinderknecht, H. Sio, A. B. Zylstra, R. D. Petrasso, P. A. Amendt, H. S. Park, B. A. Remington, D. D. Ryutov, S. C. Wilks *et al.*, *Nat. Commun.* **7**, 13081 (2016).
- [34] H.-K. Chung, M. H. Chen, W. L. Morgan, Y. Ralchenko, and R. W. Lee, *High Energy Density Phys.* **1**, 3 (2005).
- [35] J. F. Myatt, W. Rozmus, V. Y. Bychenkov, and V. T. Tikhonchuk, *Phys. Rev. E* **57**, 3383 (1998).
- [36] M. Hoshino, *Astrophys. J. Lett.* **868**, L18 (2018).
- [37] W. Fox, D. B. Schaeffer, M. J. Rosenberg, G. Fiksel, J. Matteucci, H.-S. Park, A. F. A. Bott, K. Lezhnin, A. Bhattacharjee, D. Kalantar, B. A. Remington, D. Uzdensky, C. K. Li, F. H. Séguin, and S. X. Hu, [arXiv:2003.06351](https://arxiv.org/abs/2003.06351).

- [38] J. D. Huba and L. I. Rudakov, *Phys. Rev. Lett.* **93**, 175003 (2004).
- [39] P. A. Cassak, Y.-H. Liu, and M. A. Shay, *J. Plasma Phys.* **83**, 715830501 (2017).
- [40] F. Chen, *Introduction to Plasma Physics and Controlled Fusion* (Springer, Berlin, 2016).
- [41] D. Biskamp, *Phys. Fluids* **29**, 1520 (1986).
- [42] A. Bhattacharjee, Y.-M. Huang, H. Yang, and B. Rogers, *Phys. Plasmas* **16**, 112102 (2009).
- [43] R. Samtaney, N. F. Loureiro, D. A. Uzdensky, A. A. Schekochihin, and S. C. Cowley, *Phys. Rev. Lett.* **103**, 105004 (2009).
- [44] S. Wang, L.-J. Chen, M. Hesse, D. J. Gershman, J. Dorelli, B. Giles, R. B. Torbert, C. J. Pollock, B. Lavraud, R. Strangeway, R. E. Ergun, J. Burch, L. Avanov, T. E. Moore, and Y. Saito, *Geophys. Res. Lett.* **43**, 4850 (2016).
- [45] S. Zenitani, I. Shinohara, T. Nagai, and T. Wada, *Phys. Plasmas* **20**, 092120 (2013).